RSC Advances

PAPER

View Article Online
View Journal | View Issue

Cite this: *RSC Adv.*, 2018, **8**, 15222

A facile one-step hydrothermal approach to synthesize hierarchical core–shell $NiFe_2O_4$@$NiFe_2O_4$ nanosheet arrays on Ni foam with large specific capacitance for supercapacitors†

Xinyang Zhang, Ziqing Zhang, Shuanggan Sun, Yunpeng Wu, Qiushi Sun and Xiaoyang Liu *

Received 24th March 2018
Accepted 12th April 2018

DOI: 10.1039/c8ra02559b

rsc.li/rsc-advances

In this contribution, $NiFe_2O_4$@$NiFe_2O_4$ nanosheet arrays (NSAs) with three-dimensional (3D) hierarchical core–shell structures were synthesized by a facile one-step hydrothermal method and they were used as electrode materials for supercapacitors (SCs). The $NiFe_2O_4$@$NiFe_2O_4$ composite electrode showed a high specific capacitance of 1452.6 F g^{-1} (5 mA cm^{-2}). It also exhibited a superior cycling stability (93% retention after 3000 cycles). Moreover, an asymmetric supercapacitor (ASC) was constructed utilizing $NiFe_2O_4$@$NiFe_2O_4$ NSAs and activated carbon (AC) as the positive and negative electrode, respectively. The optimized ASC shows extraordinary performances with a high energy density of 33.6 W h kg^{-1} at a power density of 367.3 W kg^{-1} and an excellent cycling stability of 95.3% capacitance retention over 3000 cycles. Therefore, $NiFe_2O_4$@$NiFe_2O_4$ NSAs have excellent pseudocapacitance properties and are good electrode materials for high energy density.

Introduction

With the continuous development of science and technology, the demand for electric energy is increasing. Therefore, higher electric energy storage is urgently needed. Tremendous efforts have been made to design and develop advanced energy storage devices.[1–4] In recent years, supercapacitors (SCs) have been becoming promising and efficient energy storage devices due to their high power density, long cycling life and fast recharge capability.[5–7] According to charging and storage mechanisms, SCs can be divided into two classes: electric double-layer capacitors (EDLCs) and pseudocapacitors.[8] Pseudocapacitors which utilize the fast reversible redox faradaic reaction of the electrode materials can provide 2–3 times higher specific capacitance than EDLCs.[9–12] In this respect, various high-performance electrode materials for pseudocapacitors, including conductive polymers,[13–15] transition metal oxides,[16–19] hydroxides,[20–22] and sulfides[23–25] have been investigated in the past few years. As the most promising candidates, ternary transition metal oxides such as $ZnFe_2O_4$,[26,27] $CoFe_2O_4$,[28,29] $NiFe_2O_4$,[30–32] $CuFe_2O_4$,[33,34] *etc.*, have received considerable attention because of their low cost, natural abundance and environmental compatibility. In particular, ternary nickel ferrite ($NiFe_2O_4$) can be utilized as an electrode material for high performance SCs due to it exhibits better electrical conductivity and electrochemical performance than those of binary nickel oxide (NiO) and iron oxide (Fe_2O_3).[35]

However, due to the low electrical conductivity and relatively small surface areas of transition metal oxides, the kinetics was limited in the redox reaction.[36,37] To further improve the specific surface areas of these materials and achieve high specific capacitance, rational design of core–shell nanoarchitectures electrodes on conductive substrates as additive/binder-free electrodes became an attractive strategy.[38–41] For instance, You *et al.* synthesized Co_3O_4/$ZnFe_2O_4$ hollow nanocomposite with a novel starfish-shaped structure by a simple hydrothermal method, of which a high specific capacitance of 326 F g^{-1} at 1 A g^{-1} was achieved and a good electrochemical cycling stability (80.7% retention after 1000 cycles) was showed.[42] According to Zhang *et al.*, the hierarchical $NiCo_2O_4$@$MnMoO_4$ core–shell nanoflowers were synthesized by the hydrothermal method, which showed a good electrochemical performance with specific capacitance of 1118 F g^{-1} at 1 A g^{-1}, and extraordinary cycling stability (only 12.15% electrochemical performance loss after 5000 cycles).[43] More recently, a three dimensional (3D) $NiCo_2O_4$@$NiCo_2O_4$ core–shell nanoflake arrays were synthesized by Tu *et al.* using a two-step hydrothermal method, which exhibited a high capacitance of 1.55 F

State Key Laboratory of Inorganic Synthesis and Preparative Chemistry, College of Chemistry, Jilin University, Changchun 130012, China. E-mail: liuxy@jlu.edu.cn; Fax: +86-0431-85168316; Tel: +86-0431-85168316

† Electronic supplementary information (ESI) available. See DOI: 10.1039/c8ra02559b

cm^{-2} at a current density of 2 mA cm^{-2}, and a high electrochemical performance retention rate of 98.6% over 4000 cycles.[39]

To the best of our knowledge, the core–shell nanomaterials were traditionally fabricated *via* two steps, by "core" formation on a conductive substrate *via* electrodeposition or hydrothermal method, and a subsequent "shell" growth step on the surface of the "core". In this work, we presented a facile one-step synthesis method to fabricate hierarchical $NiFe_2O_4$@$NiFe_2O_4$ core–shell NSAs on Ni foam as binder-free electrode. It was showed that the nanostructure of $NiFe_2O_4$@$NiFe_2O_4$ hierarchical core–shell nanosheets can be controlled by simply tuning the reaction time. As expected, the $NiFe_2O_4$@$NiFe_2O_4$ with the unique core–shell nanostructure manifested high faradaic capacitance as an additive/binder-free electrode for SCs. In addition, we had constructed an asymmetric supercapacitor (ASC) with $NiFe_2O_4$@$NiFe_2O_4$ NSAs as the positive electrode and AC as the negative electrode. The optimized ASC exhibited a high energy density of 33.6 W h kg^{-1} at the power density of 367.3 W kg^{-1}, and outstanding cycling stability (95.3% of retention of initial electrochemical performance) after 3000 cycles, indicative of its great potential in high-performance SC applications.

Experimental

Preparation of hierarchical $NiFe_2O_4$@$NiFe_2O_4$ core–shell NSAs on Ni foam

Prior to the synthesis, Ni foam (length × width × thickness = 2 cm × 1 cm × 1.6 mm) were prepared and ultrasonicated cleaned using 3 M HCl solution, deionized water, acetone, and ethanol in sequence to eliminate the possible nickel oxide layer on the surface. $NiFe_2O_4$@$NiFe_2O_4$ NSAs were synthesized on Ni foam by a facile one-step hydrothermal process. 3 mmol of $Ni(NO_3)_2 \cdot 6H_2O$, 2 mmol of $Fe_3(SO_4)_2 \cdot 7H_2O$, 8 mmol of NH_4F and 12 mmol of $CO(NH_2)_2$ were dissolved in 100 mL deionized water. The solution was stirred at room temperature and a yellow solution was obtained. The solution was then transferred to a Teflon-lined stainless steel autoclave and the pretreated Ni foam was immersed into the solution. Subsequently, the autoclave was heated to 100 °C in an airflow electric oven for 2 h, 4 h and 6 h, respectively. After cooling down naturally, the Ni foam was taken out and rinsed with distilled water and alcohol, and it was annealed at 500 °C for 3 h (heating rate of 5 °C min^{-1}). Then the $NiFe_2O_4$@$NiFe_2O_4$ NSAs could be obtained on the Ni foam surface. The composites obtained with different reaction time of 2 h, 4 h and 6 h were denoted as NFNF-2, NFNF-4 and NFNF-6. Scheme 1 schematically illustrated the fabrication of the $NiFe_2O_4$@$NiFe_2O_4$ NSAs on the surface Ni foam surface *via* our proposed one-step hydrothermal method.

Materials characterization

The morphology of the $NiFe_2O_4$@$NiFe_2O_4$ NSAs was characterized by field-emission scanning electron microscopy (SEM, JEOL JSM 6700F) and transmission electron microscopy (TEM, FEI Tecnai G2 F20 S-Twin D573) with acceleration voltage of 200 kV. The energy dispersive X-ray spectroscopy (EDS) spectra were also acquired using a JEOL JSM 6700F microscope. The composition and structure of $NiFe_2O_4$@$NiFe_2O_4$ NSAs were examined by powder X-ray diffraction (XRD, Rigaku D/Max 2550V/PC, Japan Cu-Kα radiation, λ = 0.15418 nm), and further confirmed by X-ray photoelectron spectroscopy (XPS, ESCALAB 250).

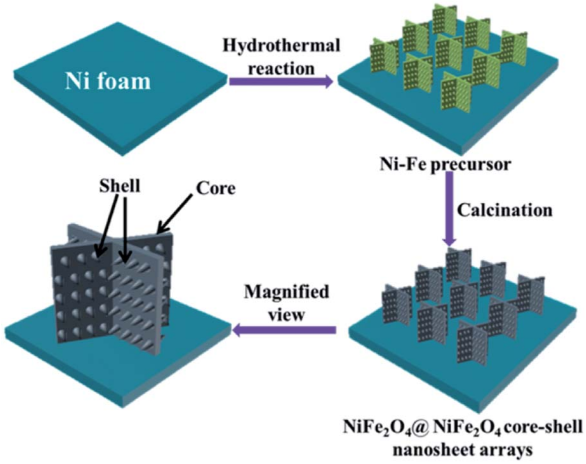

Scheme 1 Synthesis procedure of the $NiFe_2O_4$@$NiFe_2O_4$ core–shell NSAs on the surface Ni foam.

Electrochemical characterization

The electrochemical properties of as-prepared electrodes were measured on a CHI 760E electrochemical workstation using a three-electrode system in a 2 M KOH solution. Three-electrode system was consisted of a platinum counter electrode, a saturated calomel electrode (SCE) and the as-prepared hierarchical $NiFe_2O_4$@$NiFe_2O_4$ NSAs on Ni foam (1 cm × 1 cm), and they acted as the counter electrode, the reference electrode and the working electrode, respectively.

Fabrication of $NiFe_2O_4$@$NiFe_2O_4$//AC ASC

The ASC device was fabricated with $NiFe_2O_4$@$NiFe_2O_4$ NSAs as the positive electrode, AC as the negative electrode, and the 2 M KOH solution was used as the electrolyte. The specific capacitance, energy densities and power densities of the assembled ASC device were all calculated based on the total mass of both the $NiFe_2O_4$@$NiFe_2O_4$ and AC electrodes.

Results and discussion

Representative XRD and XPS patterns of the hierarchical $NiFe_2O_4$@$NiFe_2O_4$ NSAs were shown in Fig. 1. To eliminate the influence of the Ni foam, the composites were scratched from the Ni foam before measurement. The XRD patterns of NFNF-2, NFNF-4 and NFNF-6 were shown in Fig. 1a, all the peaks can be readily indexed to the monoclinic $NiFe_2O_4$ phase (JCPDS card no. 10-0325), indicating all the three samples were $NiFe_2O_4$.[44] XPS was carried out to further investigate the surface information of the $NiFe_2O_4$@$NiFe_2O_4$ NSAs (Fig. 1b–d). As can be seen in

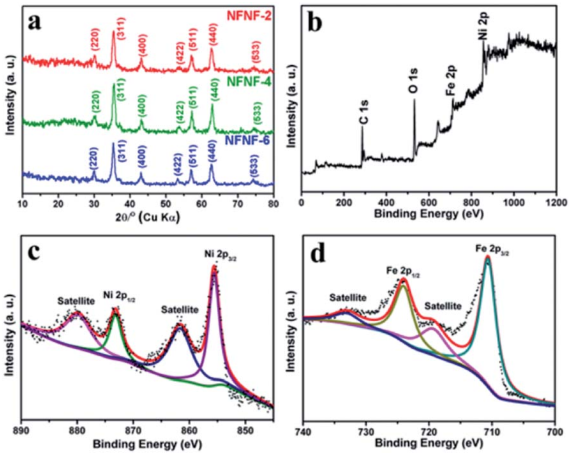

Fig. 1 (a) XRD pattern of hierarchical $NiFe_2O_4$@$NiFe_2O_4$ NSAs scratched from Ni foam; XPS spectra of (b) survey spectrum; (c) Ni 2p; (d) Fe 2p.

the survey scan of as-prepared hierarchical $NiFe_2O_4$@$NiFe_2O_4$ NSAs (Fig. 1b), the peaks of Ni, Fe and O were observed. Fig. 1c showed that the Ni 2p spectra. The peaks at 873.4 eV and 855.2 eV can be assigned to Ni $2p_{1/2}$ and Ni $2p_{3/2}$, respectively, which exhibited an separation of 18.2 eV consistent with the previously report.[45] The Fe 2p XPS pattern (Fig. 1d) showed two peaks at 725.4 and 711.8 eV, which could be assigned to the binding energy of Fe $2p_{1/2}$ and Fe $2p_{3/2}$, respectively, suggesting of the existence of Fe^{3+}.[46]

To explore the morphologies of the $NiFe_2O_4$@$NiFe_2O_4$ NSAs prepared with a different hydrothermal reaction time, the SEM was characterized and the images were collected and shown in Fig. 2. Within a short time (2 h), a number of the tiny $NiFe_2O_4$ nanoparticles appeared on the surface of the $NiFe_2O_4$ NSAs, acting as the ideal conductive scaffolds. After hydrothermal treatment for 4 h (Fig. 2b), the ultrathin $NiFe_2O_4$ nanoflakes were formed and uniformly covered on the surface of the $NiFe_2O_4$ nanosheets, developing a unique hierarchical core–shell $NiFe_2O_4$@$NiFe_2O_4$ NSAs with approximately 1.9 μm wide and 210 nm thick. The hierarchical core–shell NSAs interconnected with each other, and thus a highly porous structure was formed resulting in a large specific surface area, which was beneficial for the electrolyte penetration and ion transportation.[47] When the reaction time extended to 6 h (Fig. 2c), the $NiFe_2O_4$ nanoflakes gradually occupied the free space between the "core" sheets and almost completely covered the surface of $NiFe_2O_4$ nanosheets. In order to obtain the uniform of the core–shell structure of $NiFe_2O_4$@$NiFe_2O_4$ NSAs on Ni foam, the low magnification SEM was measured and the images were shown in Fig. S1.†

The corresponding TEM images in Fig. 3a–c also revealed the growth process of the $NiFe_2O_4$@$NiFe_2O_4$ NSAs. As shown in Fig. 3b, the $NiFe_2O_4$ core nanosheets were composed of $NiFe_2O_4$ nanoflakes of 37 nm in length. Moreover, the representative HRTEM image in Fig. 3d showed that the NFNF-4 NSAs had a set of lattice fringes with interplanar distance of 0.26 nm, well corresponding to the (311) plane of cubic spinel $NiFe_2O_4$ (JCPDS card no. 10-0325). To further verify the elemental distribution in the electrode material, the EDS mapping image was obtained and shown in Fig. 3e–h. The results indicated that the Ni, Fe, O elements were uniformly distributed throughout the core–shell nanostructure. Furthermore, the EDS pattern also confirmed the presence of Ni and Fe with an atomic ratio of about 1 : 2 (Fig. S2†).

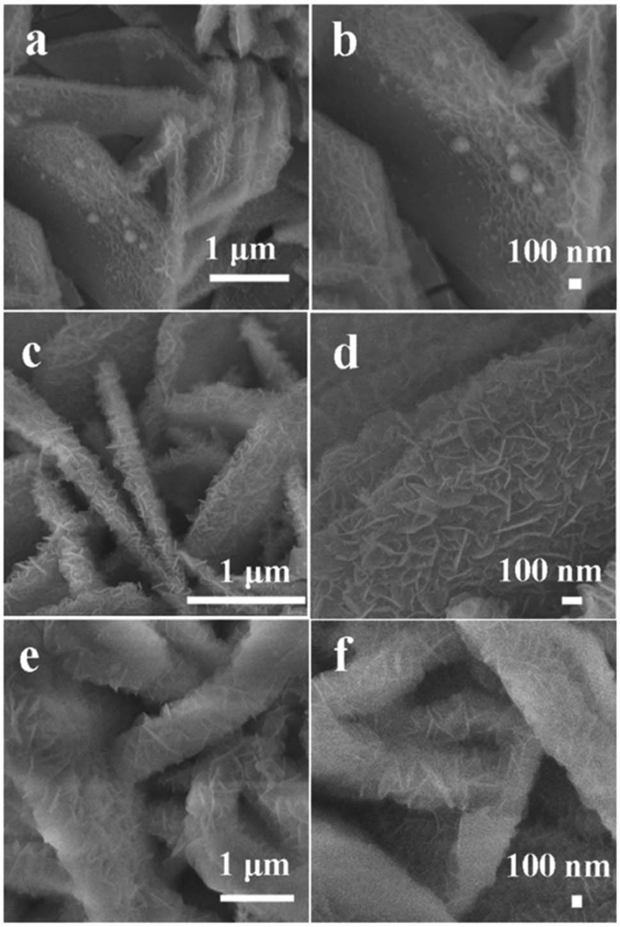

Fig. 2 SEM images of (a and b) NFNF-2; (c and d) NFNF-4; (e and f) NFNF-6 NSAs grown on Ni foam.

Electrochemical performance of $NiFe_2O_4$@$NiFe_2O_4$ NSAs

Electrochemical characterizations of NFNF-2, NFNF-4 and NFNF-6 as electrode materials for SCs were carried out by using the three-electrode system in 2 M KOH aqueous solutions (Fig. 4). The cyclic voltammetry (CV) comparison curves of NFNF-2, NFNF-4 and NFNF-6 at the same scanning rate (5 mV s^{-1}) and in the same potential window (−0.2 to 0.8 V) were shown in Fig. 4a. As shown in Fig. 4a, each of the CV curves had a pair of obvious redox peaks, suggesting of the presence of a faradaic reaction. During the charge–discharge process of electrode materials, the mechanism of redox reaction can be represented as the following reaction:[31]

$$NiFe_2O_4 + H_2O + OH^- \leftrightarrow NiOOH + 2FeOOH + e^-$$

Furthermore, the CV-integral area of the NFNF-4 electrode was higher than those of NFNF-2, NFNF-6 electrodes,

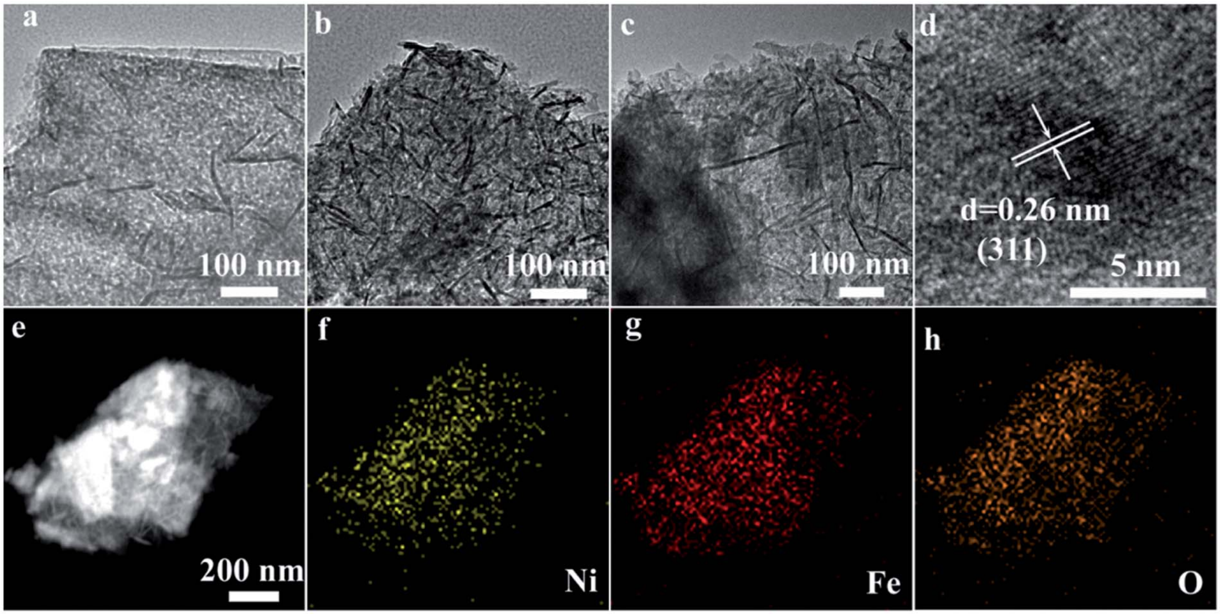

Fig. 3 TEM characterization. (a) NFNF-2; (b) NFNF-4; (c) NFNF-6; (d) HRTEM image of NFNF-4 NSAs; (e) EDS of element: (f) Ni, (g) Fe and (h) O.

demonstrating a significant increase of the areal capacitance. This fact could also be further evidenced by the CD measurements at the same current density (10 mA cm^{-2}) in Fig. 4b. Evidently, the CD curves of NFNF-2, NFNF-4 and NFNF-6 showed a good symmetry, indicating an excellent reversibility. Besides, the CD curve of the NFNF-4 electrode had the longest discharging time, exhibiting the most extraordinary pseudocapacitivity among the three electrodes, which was consistent with the above CV analysis.

Fig. 4c showed the CV curves of the NFNF-4 NSAs electrode for supercapacitor with a same potential range of −0.2 to 0.8 V at various scan rates from 5 to 60 mV s^{-1}. Specifically, a pair of similar redox peaks was observed in all the CV curves, implying that a high-rate faradaic redox reaction happened on the electrode. The NFNF-4 NSAs displayed a pair of redox peaks at 0.520 V and 0.275 V at a slow scan rate of 5 mV s^{-1}. As the scan rate gradually increased, the peak current increased and shape of the CV curves were slightly change, indicating that electrode materials could provide or accept electrons through redox reactions.[48] The electrochemical characterizations of the NFNF-4 NSAs was further confirmed by CD measurements at current densities of 5, 10, 20, 40 and 60 mA cm^{-2} (Fig. 4d). For comparison, the detailed CV and CD measures of the NFNF-2 and NFNF-6 composite electrodes were shown in Fig. S3.†

The mass specific capacitance and areal specific capacitance of the NFNF-2, NFNF-4, and NFNF-6 NSAs electrodes were calculated from the discharge time by the following equations:

$$C_\mathrm{m} = I \times \Delta t / m \times \Delta V \tag{1}$$

$$C_\mathrm{a} = I \times \Delta t / S \times \Delta V \tag{2}$$

where C_m and C_a were the mass specific capacitance and the areal specific capacitance, respectively. I was the discharge current, Δt was the discharge time, m was the total mass of the active material in the electrode, ΔV was the voltage interval and S was the geometrical area of the electrode. The corresponding results of these electrodes were presented in Fig. 4e–f. Impressively, the NFNF-4 electrode possessed high mass specific capacitances of 1451.5, 1377.4, 1274.5, 1164.7 and 923.6 F g^{-1},

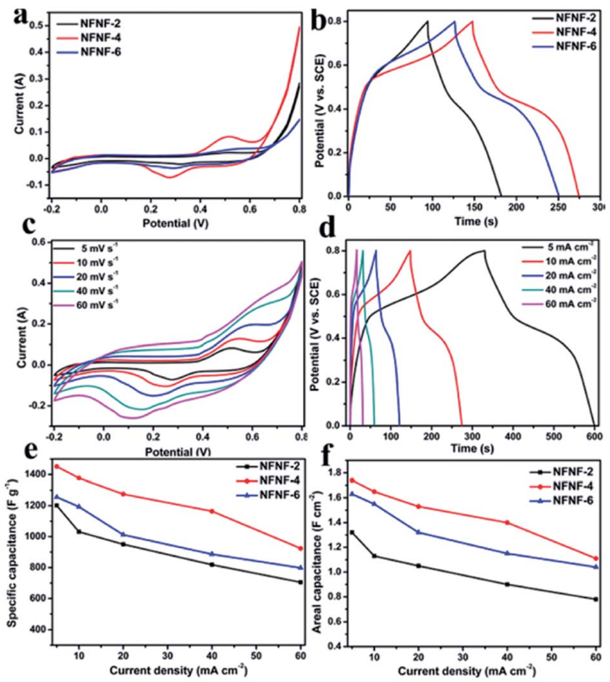

Fig. 4 Electrochemical performance measurements: comparison diagrams for (a) CV curves of NFNF-2, NFNF-4, NFNF-6 NSAs at 5 mV s^{-1}; (b) CD curves of NFNF-2, NFNF-4, NFNF-6 NSAs at 10 mA cm^{-2}; (c) CV curves of the NFNF-4 at various scan rates; (d) CD curves of NFNF-4 at different current densities; (e) specific capacitance and (f) areal capacitance of NFNF-2, NFNF-4, NFNF-6 NSAs *versus* current increase.

and high areal specific capacitances of 1.74, 1.65, 1.53, 1.40 and 1.11 F cm^{-2} at current densities of 5, 10, 20, 40 and 60 mA cm^{-2}, respectively. Nevertheless, the NFNF-2 and NFNF-6 electrodes only showed 1.13 F cm^{-2} (1031.6 F g^{-1}) and 1.55 F cm^{-2} (1193.1 F g^{-1}) at 10 mA cm^{-2}. In addition, the detailed comparison results of NFNF-2, NFNF-4 and NFNF-6 electrodes were summarized in the Table S1.† The results were much better than previously reported values of $NiFe_2O_4$ nanostructures, such as $CoFe_2O_4/NiFe_2O_4$ nanocomposites (269 F g^{-1} at 1 A g^{-1}),[49] $NiFe_2O_4/MoS_2$ composite material (506 F g^{-1} at 1 A g^{-1}),[50] $NiFe_2O_4$ nanostructures (541 F g^{-1} at 2 mV s^{-1}),[51] and $NiFe_2O_4$/PANI nanocomposites (448 F g^{-1} at 1 mA cm^{-2}).[52] The superior eletrochemical performance of the NFNF-4 electrode could be attributed to the following structural features. Firstly, the unique additive/binder-free electrode material growing on the Ni foam could significantly eliminate the "dead surface". Owing to its high electrical conductivity, the fabrication process was significantly simplified and the electron transportation during the charge–discharge process was largely enhanced. Secondly, the highly open 3D hierarchical porous structure largely shortened the electron and ion transfer pathway, increased the contact area with the electrolyte, and provided a buffering cushion to accommodate for the local volumetric expansion/contraction during long-term cycling. Nyquist plots of NFNF-2, NFNF-4 and NFNF-6 NSAs were taken in the frequency range from 0.01 Hz to 100 kHz under open circuit potential (OCP) were shown in Fig. S4.†

The cycling performance of the NFNF-2, NFNF-4, and NFNF-6 NSAs were also investigated to further evaluate the potential to serve as electrode materials for SCs. As depicted in Fig. 5, cycling stability tests for the NFNF-2, NFNF-4 and NFNF-6 NSAs were performed by measuring the retention rates of their initial capacitances over 5000 cycles at a current density of 10 mA cm^{-2}. After 5000 cycles, the specific capacitance retention rates of the three electrodes were all above 79%. The specific capacitance retention rate of the NFNF-4 electrode (1241.2 F g^{-1}, 90.2% retention) was the highest among the three electrodes, demonstrating the superior electrochemical stability originated from the three-dimensional core–shell structure. Fig. S5 and S6† showed the SEM and Nyquist plots of $NiFe_2O_4$@$NiFe_2O_4$ core–shell NSAs after 5000 cycling tests. We can observe that the morphology of the core–shell nanosheet arrays retained almost intact, which further demonstrated its high stability.

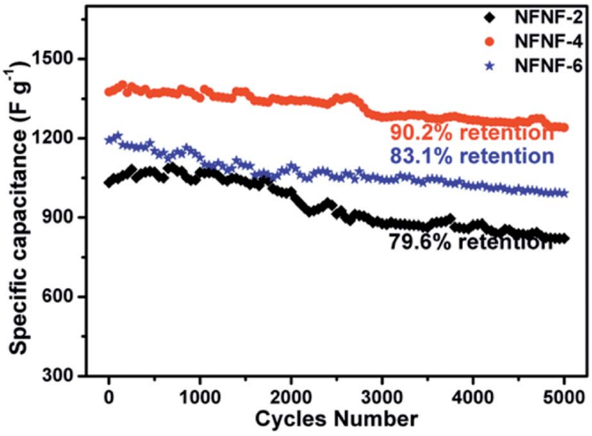

Fig. 5 Cycling performance of NFNF-2, NFNF-4, NFNF-6 NSAs at 10 mA cm^{-2}.

Electrochemical performance of the $NiFe_2O_4$@$NiFe_2O_4$//AC ASC

An ASC was assembled utilizing $NiFe_2O_4$@$NiFe_2O_4$ NSAs as the positive electrode and AC as the negative electrode in 2 M KOH electrolyte, to further confirm the extraordinary electrochemical performance that could be potentially applied in practical applications (Fig. 6a). Fig. 6b showed the CV curves of NFNF-4 and AC electrodes using a three-electrode system at a scan rate of 5 mV s^{-1}. It can be seen that NFNF-4 was measured within a potential window of 0 to 0.8 V, and AC electrode within a potential window of −1.0 to 0 V. The CV curve of AC electrode exhibited a nearly ideal rectangular shape without any redox peaks, demonstrating a typical characteristic of EDLC behavior.[53] Based on these results, the total potential window of the assembled ASC could be extended to 0–1.8 V. From the CV curves of the ASC device (Fig. 6c) recorded at different scan rates of 5–60 mV s^{-1}, it was found that the overall capacitance of the $NiFe_2O_4$@$NiFe_2O_4$//AC ASC device was a result from the combination of both faradaic pseudocapacitance and EDLC-type capacitance. Fig. 6d showed the CD curves of the ASC device at current densities of 2–40 mA cm^{-2} with the potential

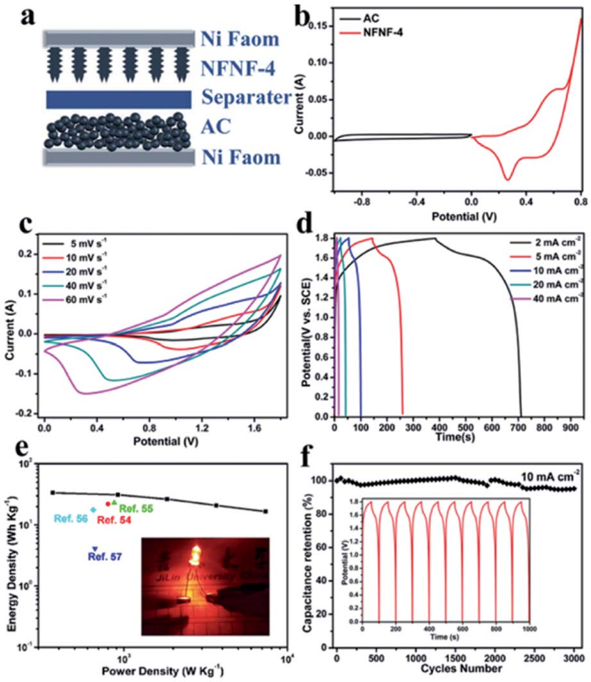

Fig. 6 (a) Schematic illustration of the $NiFe_2O_4$@$NiFe_2O_4$//AC ASC device in 2 M KOH electrolyte; (b) CV curves of the AC and $NiFe_2O_4$@$NiFe_2O_4$ electrodes at a scan rate of 5 mV s^{-1}; (c) CV curves at scan rates range from 5–60 mV s^{-1}; (d) CD curves at current densities range from 2–40 mA cm^{-2}; (e) Ragone plot; inset shows the red LED lit by two ASC devices in series; (f) cycling performance at 10 mA cm^{-2}; inset shows the CD curves of the last 10 cycles.

window of 0–1.8 V. Ragone plot relative to the corresponding energy density (E) and power density (P) were calculated as follows:

$$E = C \times \Delta V^2/7.2 \tag{3}$$

$$P = 3600 \times E/\Delta t \tag{4}$$

where E, P, C, ΔV and Δt were energy density, power density, specific capacitance, cell voltage, (s) and discharging time, respectively. (Fig. 6e). The maximum energy density (33.6 W h kg^{-1}) was achieved at a power density of 367.3 W kg^{-1}, and maintained at 16.6 W h kg^{-1} with a high power density of 7346.9 W kg^{-1}. The energy density of $NiFe_2O_4$@$NiFe_2O_4$//AC ASC device was higher than the previous reported ASC, for instance, the Co–Fe LDH@NiO–Ni//AC (22 W h kg^{-1}),[54] $NiFe_2O_4$/CNT//N-doped graphene (23 W h kg^{-1}),[55] $Ni(OH)_2$//Fe_2O_3/RGO/Fe_3O_4 (4.1 W h kg^{-1})[56] and Ni–Fe LDH/GHA (17.6 W h kg^{-1}).[57] In the next experiment, two $NiFe_2O_4$@$NiFe_2O_4$//AC devices in series successfully lit up a 5 mm diameter red LED, as shown in the inset of the Fig. 6e. The cycle life of the $NiFe_2O_4$@$NiFe_2O_4$//AC ASC device was also measured and shown in Fig. 6f. The capacitance of the ASC maintained above 95.3% of the initial value after 3000 cycles at current density of 10 mA cm^{-2}, demonstrating its superior cycling stability. Moreover, the inset of Fig. 6f showed highly similar symmetric shape of CD curves for the last ten cycles, also indicating that the ASC device possessed an extraordinary cycling stability. All these attractive results proved that the $NiFe_2O_4$@$NiFe_2O_4$//AC ASC device had an outstanding electrochemical performance and a great application potential.

Conclusions

In summary, we have controlled synthesized the hierarchical $NiFe_2O_4$@$NiFe_2O_4$ core–shell NSAs directly on Ni foam as a additive/binder-free electrode by a facile one-step hydrothermal. The as-prepared $NiFe_2O_4$@$NiFe_2O_4$ NSAs showed an extraordinary performance with a high specific capacitance for 1377.4 F g^{-1} (1.65 F cm^{-2}) at 10 mA cm^{-2}, together with an excellent cycling stability of 90.2% retention rate at a high current density of 10 mA cm^{-2} over 5000 cycles. In addition, the ASC device had been assembled by the $NiFe_2O_4$@$NiFe_2O_4$ NSAs and AC, which exhibited a high energy density of 33.6 W h kg^{-1} at a power density of 367.3 W kg^{-1}. The $NiFe_2O_4$@$NiFe_2O_4$ NSAs was a promising electrode material candidate that could be well applied in the field of renewable energy storage.

Conflicts of interest

There are no conflicts to declare.

Acknowledgements

This work was supported by the National Sciences Foundation of China (No. 21271082 and 21371068).

References

1 A. S. Aricò, P. Bruce, B. Scrosati, J. M. Tarascon and W. Van Schalkwijk, *Nat. Mater.*, 2005, **4**, 366–377.
2 M. Armand and J. M. Tarascon, *Nature*, 2008, **451**, 652–657.
3 N. S. Choi, Z. Chen, S. A. Freunberger, X. Ji, Y. K. Sun, K. Amine, G. Yushin, L. F. Nazar, J. Cho and P. G. Bruce, *Angew. Chem., Int. Ed.*, 2012, **51**, 9994–10024.
4 J. Jiang, Y. Li, J. Liu, X. Huang, C. Yuan and X. W. D. Lou, *Adv. Mater.*, 2012, **24**, 5166–5180.
5 T. Brezesinski, J. Wang, S. H. Tolbert and B. Dunn, *Nat. Mater.*, 2010, **9**, 146–151.
6 C. Liu, F. Li, L. P. Ma and H. M. Cheng, *Adv. Mater.*, 2010, **22**, E28–E62.
7 J. R. Miller and P. Simon, *Science*, 2008, **321**, 651–652.
8 X. Lang, A. Hirata, T. Fujita and M. Chen, *Nat. Nanotechnol.*, 2011, **6**, 232–236.
9 X. Li and B. Wei, *Nano Energy*, 2013, **2**, 159–173.
10 S. Peng, L. Li, H. B. Wu, S. Madhavi and X. W. D. Lou, *Adv. Energy Mater.*, 2015, **5**, 1401172.
11 J. Liu, J. Jiang, C. Cheng, H. Li, J. Zhang, H. Gong and H. J. Fan, *Adv. Mater.*, 2011, **23**, 2076–2081.
12 G. Wang, L. Zhang and J. Zhang, *Chem. Soc. Rev.*, 2012, **41**, 797–828.
13 H. Mi, X. Zhang, X. Ye and S. Yang, *J. Power Sources*, 2008, **176**, 403–409.
14 J. Zhang and X. Zhao, *J. Phys. Chem. C*, 2012, **116**, 5420–5426.
15 T. Liu, L. Finn, M. Yu, H. Wang, T. Zhai, X. Lu, Y. Tong and Y. Li, *Nano Lett.*, 2014, **14**, 2522–2527.
16 Z. Lu, Z. Chang, J. Liu and X. Sun, *Nano Res.*, 2011, **4**, 658–665.
17 W. Wei, X. Cui, W. Chen and D. G. Ivey, *Chem. Soc. Rev.*, 2011, **40**, 1697–1721.
18 B. Wang, J. S. Chen, Z. Wang, S. Madhavi and X. W. D. Lou, *Adv. Energy Mater.*, 2012, **2**, 1188–1192.
19 Q. Yang, Z. Lu, X. Sun and J. Liu, *Sci. Rep.*, 2013, **3**, 3537.
20 J. Yang, C. Yu, X. Fan and J. Qiu, *Adv. Energy Mater.*, 2014, **4**, 1400761.
21 D. Yu, Y. Wang, L. Zhang, Z. X. Low, X. Zhang, F. Chen, Y. Feng and H. Wang, *Nano Energy*, 2014, **10**, 153–162.
22 Y. Zhu, C. Cao, S. Tao, W. Chu, Z. Wu and Y. Li, *Sci. Rep.*, 2014, **4**, 5787.
23 S. Peng, L. Li, C. Li, H. Tan, R. Cai, H. Yu, S. Mhaisalkar, M. Srinivasan, S. Ramakrishna and Q. Yan, *Chem. Commun.*, 2013, **49**, 10178–10180.
24 W. Chen, C. Xia and H. N. Alshareef, *ACS Nano*, 2014, **8**, 9531–9541.
25 H. Chen, J. Jiang, L. Zhang, D. Xia, Y. Zhao, D. Guo, T. Qi and H. Wan, *J. Power Sources*, 2014, **254**, 249–257.
26 S. S. Raut and B. R. Sankapal, *Electrochim. Acta*, 2016, **198**, 203–211.
27 M. M. Vadiyar, S. C. Bhise, S. S. Kolekar, J. Y. Chang, K. S. Ghule and A. V. Ghule, *J. Mater. Chem. A*, 2016, **4**, 3504–3512.
28 L. Liu, H. Zhang, Y. Mu, J. Yang and Y. Wang, *ACS Appl. Mater. Interfaces*, 2016, **8**, 1351–1359.

29 Z. Wang, W. Jia, M. Jiang, C. Chen and Y. Li, *Nano Res.*, 2016, **9**, 2026–2033.

30 G. Huang, F. Zhang, L. Zhang, X. Du, J. Wang and L. Wang, *J. Mater. Chem. A*, 2014, **2**, 8048–8053.

31 Z. Y. Yu, L. F. Chen and S. H. Yu, *J. Mater. Chem. A*, 2014, **2**, 10889–10894.

32 M. S. Javed, C. Zhang, L. Chen, Y. Xi and C. Hu, *J. Mater. Chem. A*, 2016, **4**, 8851–8859.

33 M. Zhu, D. Meng, C. Wang and G. Diao, *ACS Appl. Mater. Interfaces*, 2013, **5**, 6030–6037.

34 W. Zhang, B. Quan, C. Lee, S. K. Park, X. Li, E. Choi, G. Diao and Y. Piao, *ACS Appl. Mater. Interfaces*, 2015, **7**, 2404–2414.

35 L. Huang, D. Chen, Y. Ding, S. Feng, Z. L. Wang and M. Liu, *Nano Lett.*, 2013, **13**, 3135–3139.

36 X. Wang, X. Han, M. Lim, N. Singh, C. L. Gan, M. Jan and P. S. Lee, *J. Phys. Chem. C*, 2012, **116**, 12448–12454.

37 G. Q. Zhang, H. B. Wu, H. E. Hoster, M. B. Chan Park and X. W. D. Lou, *Energy Environ. Sci.*, 2012, **5**, 9453–9456.

38 X. Xia, J. Tu, Y. Zhang, X. Wang, C. Gu, X. b. Zhao and H. J. Fan, *ACS Nano*, 2012, **6**, 5531–5538.

39 X. Liu, S. Shi, Q. Xiong, L. Li, Y. Zhang, H. Tang, C. Gu, X. Wang and J. Tu, *ACS Appl. Mater. Interfaces*, 2013, **5**, 8790–8795.

40 K. Xu, R. Zou, W. Li, Q. Liu, X. Liu, L. An and J. Hu, *J. Mater. Chem. A*, 2014, **2**, 10090–10097.

41 Q. Yang, Z. Lu, T. Li, X. Sun and J. Liu, *Nano Energy*, 2014, **7**, 170–178.

42 X. W. Hu, S. Liu, B. T. Qu and X. Z. You, *ACS Appl. Mater. Interfaces*, 2015, **7**, 9972–9981.

43 Z. Gu and X. Zhang, *J. Mater. Chem. A*, 2016, **4**, 8249–8254.

44 J. Shao, X. Li, Y. Ding, Z. Wan, H. Liu, J. Yun, Y. Liu, Q. Qu and H. Zheng, *Electrochem. Commun.*, 2014, **40**, 9–12.

45 J. W. Lee, T. Ahn, D. Soundararajan, J. M. Ko and J. D. Kim, *Chem. Commun.*, 2011, **47**, 6305–6307.

46 Q. X. Low and G. W. Ho, *Nano Energy*, 2014, **5**, 28–35.

47 D. P. Dubal, G. S. Gund, C. D. Lokhande and R. Holze, *ACS Appl. Mater. Interfaces*, 2013, **5**, 2446–2454.

48 R. Zou, Z. Zhang, M. F. Yuen, J. Hu, C. S. Lee and W. Zhang, *Sci. Rep.*, 2015, **5**, 07862.

49 X. Feng, Y. Huang, X. Chen, C. Wei, X. Zhang and M. Chen, *J. Mater. Sci.*, 2018, **53**, 2648–2657.

50 Y. Zhao, L. Xu, J. Yan, W. Yan, C. Wu, J. Lian, Y. Huang, J. Bao, J. Qiu, L. Xu, Y. Xu, H. Xu and H. Li, *J. Alloys Compd.*, 2017, **726**, 608–617.

51 P. Bhojane, A. Sharma, M. Pusty, Y. Kumar, S. Sen and P. Shirage, *J. Nanosci. Nanotechnol.*, 2017, **17**, 1387–1392.

52 B. Senthilkumar, K. V. Sankar, C. Sanjeeviraja and R. K. Selvan, *J. Alloys Compd.*, 2013, **553**, 350–357.

53 M. D. Stoller, S. Park, Y. Zhu, J. An and R. S. Ruoff, *Nano Lett.*, 2008, **8**, 3498–3502.

54 K. Ma, F. Liu, M. Zhang, X. Zhang and J. P. Cheng, *Electrochim. Acta*, 2017, **225**, 425–434.

55 N. Kumar, A. Kumar, G.-M. Huang, W.-W. Wu and T. Y. Tseng, *Appl. Surf. Sci.*, 2018, **433**, 1100–1112.

56 C. Zhao, X. Shao, Y. Zhang and X. Qian, *ACS Appl. Mater. Interfaces*, 2016, **8**, 30133–30142.

57 X. Gao, H. Lv, Z. Li, Q. Xu, H. Liu, Y. Wang and Y. Xia, *RSC Adv.*, 2016, **6**, 107278–107285.